Biomedicine & Pharmacotherapy 176 (2024) 116768

Contents lists available at ScienceDirect

Biomedicine & Pharmacotherapy

journal homepage: www.elsevier.com/locate/biopha

Repurposing anti-cancer porphyrin derivative drugs to target SARS-CoV-2 envelope

Diogo A. Mendonça [a,1], Iris Cadima-Couto [a,1], Carolina C. Buga [a,c], Zoe A. Arnaut [a,b], Fabio A. Schaberle [b], Luis G. Arnaut [b], Miguel A.R.B. Castanho [a,*], Christine Cruz-Oliveira [a,*]

[a] Instituto de Medicina Molecular, Faculdade de Medicina, Universidade de Lisboa, Lisboa 1649-028, Portugal
[b] CQC-IMS, Chemistry Department, University of Coimbra, Coimbra 3004-535, Portugal
[c] Instituto de Tecnologia Química e Biológica António Xavier, Universidade Nova de Lisboa, Av. da República, Oeiras 2780-157, Portugal

ARTICLE INFO

Keywords:
SARS-CoV-2
Antiviral agents
Porphyrin derivatives
Verteporfin
Temoporfin
Membrane targeting

ABSTRACT

Antiviral medicines to treat COVID-19 are still scarce. Porphyrins and porphyrin derivatives (PDs) usually present broad-spectrum antiviral activity with low risk of resistance development. In fact, some PDs are clinically approved to be used in anti-cancer photodynamic therapy and repurposing clinically approved PDs might be an alternative to treat COVID-19. Here, we characterize the ability of temoporfin, verteporfin, talaporfin and redaporfin to inactivate SARS-CoV-2 infectious particles. PDs light-dependent and –independent effect on SARS-CoV-2 infectivity were evaluated. PDs photoactivation successfully inactivated SARS-CoV-2 with very low concentrations and light dose. However, only temoporfin and verteporfin inactivated SARS-CoV-2 in the dark, being verteporfin the most effective. PDs treatment reduced viral load in infected Caco-2 cells, while not inducing cytotoxicity. Furthermore, light-independent treatment with temoporfin and verteporfin act on early stages of viral infection. Using lipid vehicles as membrane models, we characterized PDs interaction to the viral envelope. Verteporfin presented the lowest IC50 for viral inactivation and the highest partition coefficients (K_p) towards lipid bilayers. Curiously, although temoporfin and redaporfin presented similar K_ps, redaporfin did not present light-independent antiviral activity, and only temoporfin and verteporfin caused lipid membrane disorder. In fact, redaporfin is located closer to the bilayer surface, while temoporfin and verteporfin are located closer to the centre. Our results suggest that viral envelope affinity, with penetration and destabilization of the lipid bilayer, seems critical to mediate PDs antiviral activity. Altogether, these findings open new avenues for the off-label application of temoporfin and verteporfin in the systemic treatment of COVID-19.

1. Introduction

The number of viral outbreaks has increased over the past decades and their frequency is expected to increase [1]. In December 2019, coronavirus disease 2019 (COVID-19) pandemic emerged in Wuhan, China and the new member of *Coronaviridae* family, severe acute respiratory syndrome coronavirus 2 (SARS-CoV-2) quickly became a global public health emergency [2,3]. Despite COVID-19 mitigation measures and vaccination efforts worldwide, anti-vaccination movements and new SARS-CoV-2 variants threaten vaccine efficacy and disease control. Moreover, new variants of SARS-CoV-2 emerge at high pace. Thus, it is of upmost importance to find therapeutic alternatives that efficiently target SARS-CoV-2 acute viral infections, as chemotherapies for COVID-19 are scarce.

SARS-CoV-2 is an enveloped virus with positive-sense single-stranded RNA genome, which encodes 4 structural proteins. The N proteins are associated with the genome forming the nucleocapsid, which is surrounded by the viral envelope, containing the viral spike (S), membrane (M), and envelope (E) proteins. Virus binding and entry into host cell is mediated by the S protein, which is recognized by the host receptor angiotensin-converting enzyme 2 (ACE2), and then cleaved by transmembrane proteases, such as TMPRSS2 (cell surface) or by cathepsin (endosome) for triggering viral envelope/host cell membrane fusion for viral genome release into the cytoplasm [4].

The early stages of infection are promising targets for the development of new antiviral drugs and the S protein is an obvious target for the

* Corresponding authors.
E-mail addresses: macastanho@medicina.ulisboa.pt (M.A.R.B. Castanho), christine.oliveira@medicina.ulisboa.pt (C. Cruz-Oliveira).
[1] Authors contributed equally.

https://doi.org/10.1016/j.biopha.2024.116768
Received 11 March 2024; Received in revised form 14 May 2024; Accepted 17 May 2024
Available online 24 May 2024

development of antivirals [5,6]. However, alternative molecules, such as the ones targeting the viral envelope integrity, should be considered. Such molecules are expected to have broad-spectrum activity among different enveloped viruses. At variance with conventional drugs, lipid bilayer-targeting drugs do not depend on a particular protein sequence and, as such, protein mutations cannot confer resistance.

Tetrapyrrolic macrocycles, such as porphyrins and their reduced derivatives chlorins and bacteriochlorins, are good photosensitizers and are used in photodynamic therapy (PDT) [7,8]. PDT is based on the activation of a photosensitizer by visible or near-infrared light in the presence of oxygen to generate singlet oxygen and free radicals that may be deleterious to tumour cells and pathogens [7,8]. In fact, porphyrins and porphyrin derivatives (PDs) were successfully used in antimicrobial PDT (aPDT) to inactivate several enveloped viruses with low risk of microorganism resistance development [9–17]. Moreover, porphyrins and PDs have also light-independent antiviral activity [10,11,18–27]. Our group and others have demonstrated that several porphyrins had a direct effect on viral particle envelope, more specifically at the lipid membrane level, inhibiting the early stages of viral infection [10,11,17,18,23,25].

Some PDs are approved for clinical application in PDT, including the chlorin-based temoporfin (Foscan®), talaporfin (Laserphyrin®), and verteporfin (Visudyne®) indicated for the treatment of head and neck cancer, lung cancer, and age-related macular degeneration, respectively [8,28,29]. In addition, the bacteriochlorin redaporfin is currently under clinical trials, with promising phase I/IIa POC clinical data in advanced head and neck cancer [30].

Here, we investigated anti-SARS-CoV-2 activity of temoporfin, verteporfin, talaporfin and redaporfin. Biophysical and *in vitro* infectivity assays were performed to unravel PDs anti-SARS-CoV-2 light-independent mechanism of action. Moreover, PDs cytotoxicity and therapeutic potential was assessed in Caco-2 cells. Overall, these results open new possibilities for PDs application in antiviral therapy. Importantly, the drugs do not require photoactivation for their antiviral activity and, therefore, could be used systemically.

2. Material and methods

2.1. Materials

Temoporfin, verteporfin and talaporfin were purchased from MedChemExpress (Monmouth Junction, NJ, USA). Redaporfin (LUZ11) was kindly provided by Luzitin SA (Coimbra, Portugal). All PDs were diluted in dimethyl sulfoxide (DMSO) to a stock with maximum concentration of 10 mM and frozen at - 20°C. All solutions were prepared in the dark. For the experimental procedures, PDs were diluted in culture medium or buffer, with the final DMSO concentration being maintained at 1%, which did not affect SARS-CoV-2 infectivity, cell viability or large unilamellar vesicles (LUVs) integrity (data not shown). 1-Palmitoyl-2-oleyl-sn-glycero-3-phosphatidylcholine (POPC) and 1-palmitoyl-2-oleoyl-sn-glycero-3-phosphoglycerol (POPG) were purchased from Avanti Polar Lipids (Alabaster, AL, USA). Cholesterol, Laurdan, 5-NS and 16-NS were purchased from Sigma-Aldrich (St. Louis, MO, USA).

2.2. Cell culture

Vero CCL-81 and Caco-2 cells were purchased from ATCC (Manassas, VA, USA). All cells were cultured at 37°C in a 5% CO_2 atmosphere. Vero CCL-81 cells were cultured in Dulbecco's Modified Eagle's Medium (DMEM) high glucose (Thermo-Fisher, Waltham, MA, USA) supplemented with 10% fetal bovine serum (FBS) and penicillin−streptomycin (Pen-Strep) (complete medium). Caco-2 cells were cultured in Eagle's Minimum Essential Medium (EMEM) (ATCC, Manassas, VA, USA) (Manassas, VA, USA) supplemented with 20% FBS and Pen-Strep (complete medium). FBS and Pen-Strep were obtained from Thermo-Fisher Scientific (Waltham, MA, USA).

2.3. Viruses

SARS-CoV-2 B.1.1 lineage (Portuguese isolate) was kindly provided by Pedro Simas Lab from Instituto de Medicina Molecular, Lisboa, Portugal and ZIKV PRVABC59 was purchased from ATCC (Manassas, VA, USA). Viruses were propagated in Vero CCL-81 cells. For SARS-CoV-2 infectious particles production, cells were infected using DMEM supplemented with 2.5% FBS (v/v) and 100 U/mL Pen Strep at a multiplicity of infection (MOI) of 0.01 for 1 hour. Next, the medium (DMEM supplemented with 2.5% FBS (v/v) and 100 U/mL Pen Strep) was changed and after 2–4 days, the conditioned medium containing the infectious virus particles was harvested and centrifuged at 450 x g for 15 min to remove cell debris.

For ZIKV infectious particles production, cells were infected with ZIKV using DMEM without FBS and 100 U/mL Pen Strep at a multiplicity of infection (MOI) of 0.01 for 1 hour. Next, the medium was replaced for DMEM supplemented with 2% FBS (v/v) and 100 U/mL Pen Strep and after 2–4 days, the conditioned medium containing the virus particles was harvested and centrifuged at 450 x g for 15 min to remove cell debris.

Viral stocks were then frozen at −80°C. All experiments involving SARS-CoV-2 handling and infection were performed in BSL3 conditions.

2.4. Virus quantification

Virus titre was quantified by plaque assay in Vero CCL-81 cells. Briefly, viral samples were 10-fold serially diluted in DMEM supplemented with 2.5% or without FBS (v/v) for SARS-CoV-2 or ZIKV, respectively, and incubated for 1 hour at 37 °C and 5% CO_2 with Vero CCL-81 cells. After 1 hour of infection, DMEM supplemented with 2.5% or 1% FBS (v/v), for SARS-CoV-2 or ZIKV, respectively, 100 U/mL Pen-Strep and 1.5% carboxymethylcellulose (CMC; Sigma-Aldrich, St. Louis, MO, USA) was added to the wells. Cells were kept in culture at 37°C in a 5% CO_2 atmosphere for 5 or 4 days, for SARS-CoV-2 or ZIKV, respectively. The cells were then fixed with 5% (v/v) formaldehyde solution and plaque was visualized by standard crystal violet staining. Data are represented as means of at least three different independent experiments.

2.5. PD treatment for virus inactivation

To determine the effect of temoporfin, verteporfin, talaporfin and redaporfin on SARS-CoV-2 infectious particles, 10^4-10^6 plaque forming units (PFU)/mL of virus were treated with different PD concentrations in culture medium supplemented with 2.5% FBS (v/v) and 100 U/mL Pen-Strep in the dark or under light stimuli. To determine the effect of temoporfin and verteporfin on ZIKV infectious particles, 10^4-10^6 PFU/mL of virus were treated with different PD concentrations in culture medium without FBS (v/v) and 100 U/mL Pen-Strep in the dark. For PD dark antiviral activity determination, virus samples were incubated for 1 hour at 37 °C and 5% CO_2 atmosphere in the dark. Meanwhile, in order to assess light-dependent PD antiviral activity, the photosensitizers were activated with adequate light sources. A light-emitting diode (LED) at 660 nm (KINGBO 36 W all deep red 660 nm LED), for temoporfin, talaporfin and verteporfin activation, or 750 nm (Marubeni L740–66–60–550) for redaporfin activation, were used to deliver a light dose (LD) of 0.5 J/cm^2. A power meter (Coherent LaserCheck - RoHS) was used to measure the light power (μW) applied on the samples for further LD calculation in J/cm^2. LD corrections were performed in order to deliver the actual light dose value to the samples allowing quantitative comparisons between photosensitizers and light sources. Multiplicative factors for each PD were calculated by overlapping the LED light emission spectra with the compounds absorption spectra. Thus, the measured LD was corrected by the following multiplicative factors: temoporfin = 0.65, verteporfin = 0.24, redaporfin = 0.4 and talaporfin = 0.6 [31]. After the different PDs treatment protocols, viral infectivity

was determined by plaque assay in Vero CCL-81 cells.

The half-maximal (50%) inhibitory concentration (IC50) was determined by nonlinear regression with a sigmoidal and variable slope profile using GraphPad Prism (version 8.4.3) software. Data are represented as means of at least three different independent experiments.

2.6. Cell viability determination

Cell viability was evaluated by CellTiter-Blue Cell Viability Assay (Promega, Madison, WI, USA), a resazurin reduction-based assay, distinguishing metabolic from non-metabolic active cells.

Briefly, Caco-2 cells (2.5×10^4 cells/well) were seeded in tissue culture-treated 96-well black flat-bottomed polystyrene plates (Corning, New York, NY, USA) and incubated for 48 hours at 37 °C with 5% CO_2. To determine light-independent PDs cytotoxicity, cells were treated with different concentrations of each PD in complete medium with 1% DMSO (v/v) for 24 hours in the dark at 37 °C with 5% CO_2. Alternatively, to determine light-dependent cytotoxicity, cells were incubated with different concentrations of each PD in complete medium with 1% DMSO (v/v), followed by immediate photoactivation with a LD of 0.5 J/cm^2 and incubation for 24 hours at 37 °C with 5% CO_2 in the dark. After PDs treatment, cells were washed with PBS, pH 7.4, and 15 μL of CellTiter-Blue reagent in 100 μL of complete medium was added to the cells and incubated for 2 hours at 37 °C and 5% CO_2 atmosphere. Resorufin fluorescence was measured at 590 nm, with excitation at 560 nm, using a Varioskan LUX multimode microplate reader (TermoFisher Scientific, Waltham, MA, USA). Cell incubated with complete medium and medium containing 0.25% Triton X100 were used as positive and negative controls (100% and 0% viability), respectively. % cell viability was determined using Eq. 1:

$$\%cellviability = \frac{F_t - F_b}{F_{unt} - F_b} \times 100 \quad (1)$$

where F_t is the fluorescence emission of PD-treated cells, F_{unt} is the fluorescence emission of the control untreated cells, and F_b is the fluorescent emission of CellTiter-Blue reagent in complete medium without cells (blank).

The 50% cytotoxicity concentration (CC50) was determined by nonlinear regression with a sigmoidal and variable slope profile using GraphPad Prism (version 8.4.3) software. Data are represented as means of at least three different independent experiments.

2.7. Time-of-addition and PD treatment of infected Caco-2 cells

The effects of PDs incubation at different stages of viral replication were tested using 4 different protocols: 1) cell pre-incubation with PDs, 2) virus pre-incubation with PDs, 3) PDs incubation during infection (co-incubation) and 4) PDs incubation after infection (treatment).

Briefly, Caco-2 cells ($1{,}5 \times 10^5$ cells/well) were seeded in tissue culture-treated 24-well flat-bottomed polystyrene plates (Corning, New York, NY, USA) and cultured in complete medium for 48 hours at 37 °C with 5% CO_2. Viral samples of 10^5 PFU/mL were used in the experiments. 1) For cell pre-incubation assays, cells were incubated with temoporfin, verteporfin or vehicle (EMEM 2.5% FBS (v/v) 1% DMSO (v/v) and 100 U/mL Pen-Strep) for 1 hour at 37 °C with 5% CO_2. Next, PD-treated and vehicle-treated cells (control) were infected with 200 μL of SARS-CoV-2 in EMEM 2.5% FBS (v/v) and 100 U/mL Pen-Strep for 1 hour at 37 °C with 5% CO_2. Following, the medium was replaced by complete medium and 24 hours later, virus infectivity was evaluated in the cells supernatant by plaque assay in Vero CCL-81 cells. 2) For virus pre-incubation, SARS-CoV-2 infectious particles were incubated with temoporfin, verteporfin or vehicle (EMEM 2.5% FBS (v/v) 1% DMSO (v/v) and 100 U/mL Pen-Strep) for 1 hour at 37 °C with 5% CO_2. Next, 200 μL of PD-treated or vehicle-treated (control) SARS-CoV-2 were used to infect cells for 1 hour at 37 °C with 5% CO_2. Following, the medium was replaced by complete medium and 24 hours later virus infectivity was evaluated in the cells supernatant by plaque assay in Vero CCL-81 cells. 3) For co-incubation assays, cells were infected with 200 μL of SARS-CoV-2 infectious particles in the absence (control) or presence (PD-treated) of temoporfin or verteporfin in EMEM 2.5% FBS (v/v) 1% DMSO (v/v) and 100 U/mL Pen-Strep for 1 hour at 37 °C with 5% CO_2. Following, the medium was replaced by complete medium and 24 hours later virus infectivity was evaluated in the cells supernatant by plaque assay in Vero CCL-81 cells. 4) Finally, for treatment assays, cells were infected with 200 μL of SARS-CoV-2 infectious particles (EMEM 2.5% FBS (v/v) and 100 U/mL Pen-Strep) for 1 hour at 37 °C with 5% CO_2 and then the medium was replaced by complete medium containing temoporfin or verteporfin (1% DMSO) and 24 hours later virus infectivity was evaluated in the cells supernatant by plaque assay in Vero CCL-81 cells. Data are represented as means of at least three different independent experiments.

2.8. LUV Preparation and PD-membrane Interaction Measurements

Large unilamellar vesicles (LUVs) with an average diameter of 100 nm were prepared by extrusion methods as previously described [32]. Briefly, the lipid mixture was first solubilized in chloroform in a round-bottom flask. The solvent was evaporated under nitrogen flow until a thin lipid film was formed. The lipid film was dried under vacuum overnight. A multilamellar vesicle (MLV) suspension was obtained after rehydration with the sample buffer (HEPES 10 mM 150 mM NaCl buffer) and a series of 10 freeze-thaw cycles. The MLV suspension was extruded through a 100-nm-pore-size Nuclepore polycarbonate membrane purchased from Whatman/GE Healthcare (Maidstone, United Kingdom) using a LiposoFast-Basic plus Stabilizer setup from Avestin (Mannheim, Germany), allowing the reorganization of MLVs into LUVs. POPC, POPC-POPG (4:1) and POPC-Chol (2:1) liposomes were prepared.

Lipid membrane partition experiments were performed by successive additions of LUVs (15 mM) aliquots to PDs solutions (10 μM), covering final lipid concentrations between 0 and 5 mM. A 10 min incubation period was allowed between each lipid addition. The extent of partition to lipid membranes was followed by the PDs steady-state fluorescence emission intensity, measured at each lipid concentration. Excitation and emission wavelengths used were 379 nm, collecting 600–700 nm emission spectra, 652 nm collecting 670–800 emission spectra, and 690 nm and collecting 720–820 nm emission spectra, for RD, TP and VP respectively. Excitation and emission slits were both 5 nm. Fluorescence intensity was corrected for dilution, background, and light scattering. K_p values were determined from nonlinear regression fit of Eq. 2 to experimental data:

$$\frac{I}{I_W} = \frac{1 + K_P \gamma_L \frac{I_L}{I_W}[L]}{K_P \gamma_L [L]} \quad (2)$$

in which I_W and I_L are the integrated fluorescence emission intensities in aqueous solution and in lipid, respectively, γ_L is the lipid molar volume, and *[L]* the lipid concentration [33].

Alteration of membrane order due to the PD interaction was evaluated by determination of the laurdan fluorescence spectral shift. Laurdan probe was added to the LUV solution to a final concentration of 9.9 μM, and left to incubate for 1 hour in the dark with gentle agitations every 15 min. After successive PDs addition (with a 10-min incubation time between each addition), samples were excited at 360 nm and the fluorescence emission spectra were recorded from 400 to 600 nm. Laurdan generalized polarization (GP), which represents the shift in the laurdan spectrum induced by medium polarity changes, was calculated as described in Eq. 3:

$$GP = \frac{I_{440} - I_{490}}{I_{440} + I_{490}} \quad (3)$$

where I_{440} and I_{490} are the emission intensities at 440 and 490 nm,

respectively [34,35].

PDs intramembrane depth was determined by parallax fluorescence quenching as described elsewhere [36–38]. Briefly, POPC LUVs containing 0% of lipophilic quenchers, 15% of 5-NS or 15% 16-NS lipophilic quenchers were prepared using the same procedure described above. PDs (10 μM) and 1 mM of each individual LUV solution were incubated for 1 hour. PDs fluorescence emission of each sample was followed using the same settings described earlier. PDs intramembrane depth was calculated based on Eqs. 4 and 5:

$$z_{1\,F} = \frac{\left(\frac{1}{-\pi C}\ln\frac{F_1}{F_2} - {L_{21}}^2\right)}{2L_{21}} \quad (4)$$

where, $Z_{1\,F}$ is the difference in 5-NS quencher and PDs depth, C is the concentration of quencher in molecules per unit area (mole fraction of quencher lipid in total lipid/70 Å^2) [39], F_1 is the PDs fluorescence in the presence of 5-NS quencher, F_2 is the PDs fluorescence in the presence of 16-NS quencher, and L_{21} is the difference of the two quenchers in depth. Upon determination of $Z_{1\,F}$:

$$z_{cF} = z_{1\,F} + L_{c1} \quad (5)$$

in which Z_{cF} is the difference between the PD and the lipid bilayer centre and L_{c1} is the distance from the bilayer centre to the 5-NS quencher.

All spectroscopy studies described above were conducted in a FLS920 series Edinburgh Instrument (Livingston, UK), at temperature of 25ºC. Data are represented as means of at least three different

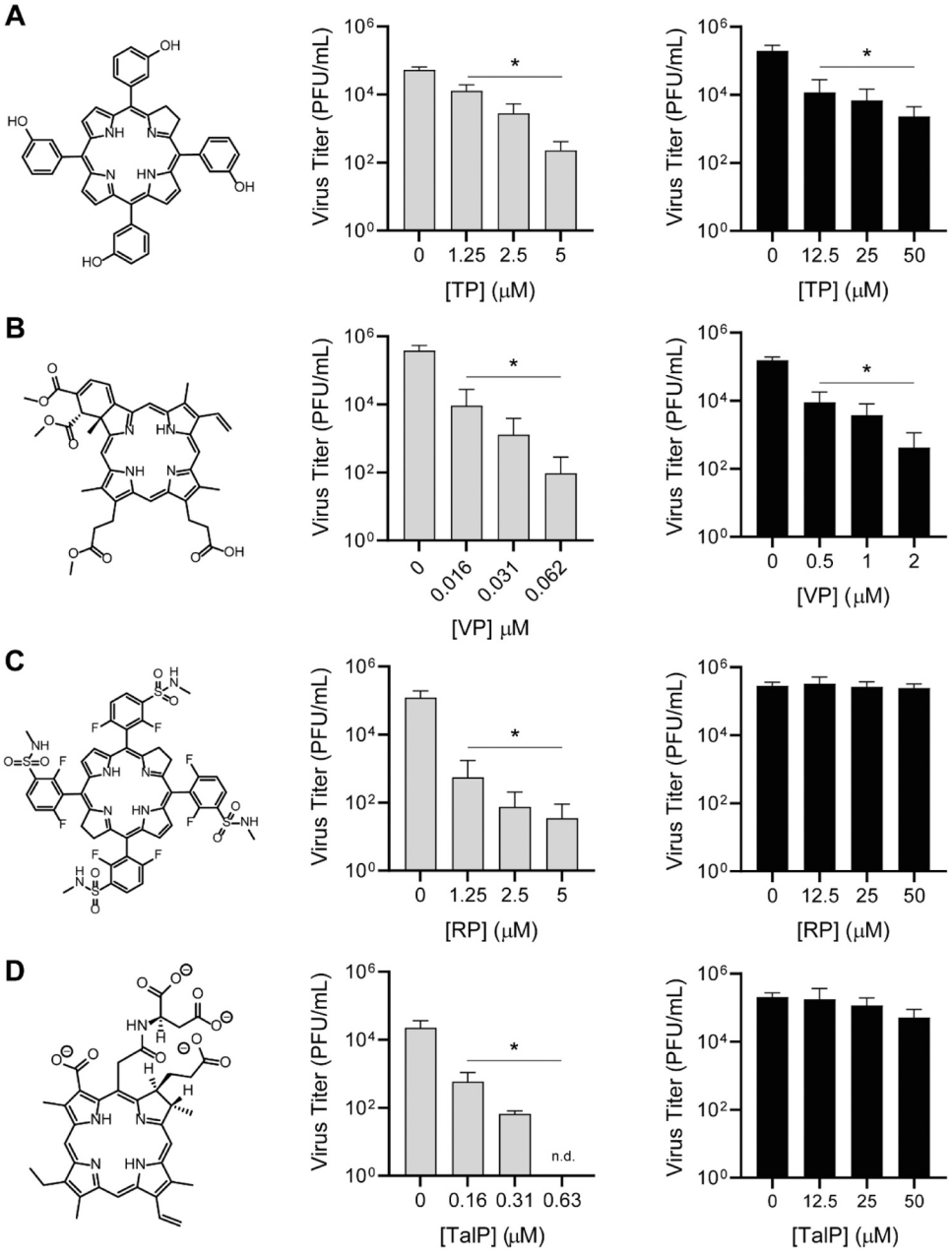

Fig. 1. SARS-CoV-2 inactivation by clinically approved PDs. (A) Temoporfin (TP), (B) verteporfin (VP), (C) redaporfin (RP) and (D) talaporfin (TalP) structures are represented (left panels). SARS-CoV-2 infectious particles were incubated with (A) TP, (B) VP, (C) RP and (D) TalP immediate followed by photoactivation with a light dose of 0.5 J/cm^2 (middle-panels). SARS-CoV-2 infectious particles were incubated with (A) TP, (B) VP, (C) RP and (D) TalP for 1 hour in the dark (right panel). Viral infectivity was evaluated by plaque assay. Data are represented as means ± SEM for at least three independent samples.* - Results with p-value ≤ 0.05 when compared with untreated group.

independent experiments.

2.9. Statistical analysis

Statistical analyses were performed using GraphPad Prism (version 8.4.3) software. One-way ANOVA was used to assess statistically significant differences between groups ($P < 0.05$).

3. Results and discussion

3.1. Photoactivated PDs successfully inactivate SARS-CoV-2 infectious particles

PDs can be used in aPDT, with low risk of developing microorganism resistance [14,40]. Therefore, we first studied the repurposing of different anti-cancer PDs in aPDT against SARS-CoV-2. For this, viral particles were directly incubated with different concentrations of temoporfin, verteporfin, talaporfin or redaporfin (Fig. 1, left panel), following immediate photoactivation (Fig. 1, middle panel and Supplementary figure 1). Infectivity yields of the treated viral particles were evaluated by plaque assay. All photoactivated PDs, using very low light dose (0.5 J/cm^2), were able to inactivate SARS-CoV-2 infectious particles with IC50s in the nanomolar range (Table 1). Verteporfin presented the lowest IC50 (3.0 ± 0.5 nM), while photoactivated temoporfin was the least effective against SARS-CoV-2 (638 ± 158 nM).

Porphyrin light-dependent antiviral activity has been studied before by our group and others [9–13,15–17]. We have previously shown that photoactivation enhanced Sn-protoporphyrin IX antiviral activity against several enveloped virus, including Zika (ZIKV), Chikungunya (CHIKV) and Vesicular Stomatitis (VSV) viruses [11]. Furthermore, singlet oxygen generated by protoporphyrin IX, mesoporphyrin IX and Zn-protoporphyrin IX causes VSV glycoprotein cross-linking and envelope protein loss, affecting viral morphology and infectivity [10]. Recently, singlet oxygen generation was also related to the inactivation of tick-born encephalitis virus by different porphyrins and PDs [17]. Likewise, a similar antiviral mechanism should be involved in SARS-CoV-2 inactivation by the photoactivated temoporfin, verteporfin, talaporfin and redaporfin. Noteworthy, aPDT of nose and lungs can be easily achieved by irradiation with an endoscopic optical fibre [14,41]. Inhibition of SARS-CoV-2 was also demonstrated with aPDT *in vitro* using PDs and methylene blue [41–44]. In fact, non-invasive aPDT using methylene blue was successfully used in COVID-19 treatment [41,45], reducing viral load and disease progression. Therefore, the repurposing of anti-cancer PDs in anti-SARS-CoV-2 aPDT appears feasible. Moreover, PD-based aPDT could be used for development of innovative technologies, e.g. photoactive textiles and auto-disinfect surfaces [14], with future positive impact on health services and industry.

Although most of the PDs used in this study are already approved in clinics, it was important to determine their CC50/IC50 ratio to estimate the safety of the studied PDs for anti-SARS-CoV-2 applications, specifically. For this, photoactivated temoporfin, verteporfin, redaporfin and talaporfin cytotoxicity was evaluated using resazurin reduction-based assays, in non-infected human intestinal Caco-2 cells 24 hours post PD photoactivation (Supplementary figure 1). For light doses of 0.5 J/cm^2, the calculated CC50 are above 50 μM for temoporfin, redaporfin and talaporfin, and 2.0 ± 0.1 μM for verteporfin (Table 1), values considered of safe prospective application given the CC50/IC50 ratios of around 666 for verteporfin, above 78 for temoporfin and above 2000 for redaporfin and talaporfin.

Table 1
CC50 and IC50 values of clinically approved PDs.

	Mean CC50 ± SEM (μM)		Mean IC50 ± SEM (nM)		
PD	**Caco-2**		**SARS-CoV-2**		**ZIKV**
	Non-PA	**PA (0.5 J/cm^2)**	**Non-PA**	**PA (0.5 J/cm^2)**	**Non-PA**
TP	> 50	> 50	1859 ± 274	638 ± 158	276 ± 64
VP	> 10	2 ± 0.1	93 ± 19	3 ± 0.5	95 ± 21
RP	> 50	> 50	N.A.*	25 ± 3	N.D.
TalP	> 50	> 50	N.A.*	22 ± 4	N.D.

PA (photoactivated), N.A. (not active), N.D. (not determined).

3.2. Temoporfin and verteporfin inactivate SARS-CoV-2 infectious particles in the dark

Although, aPDT is feasible for controlling viral infection in the airways, [41,45] light-independent PD antiviral activity is a more practical and convenient biomedical approach, allowing effective systemic treatment of SARS-CoV-2 infection. Here, we studied whether temoporfin, verteporfin, talaporfin or redaporfin also have light-independent antiviral activity. For this purpose, SARS-CoV-2 infectious particles were directly incubated with different concentrations of each PD for 1 hour in the dark. Infectivity yields of the treated viral particles were assessed by plaque assay (Fig. 1, right panel and Fig. 2). Only temoporfin and verteporfin presented light-independent anti-SARS-CoV-2 activity. Verteporfin was the most effective against SARS-CoV-2 in the dark, with an IC50 of 93 ± 19 nM while temoporfin presented an IC50 of about 1859 ± 274 nM (Table 1).

Porphyrins and PDs light-independent antiviral activity has already been demonstrated against some enveloped viruses other than SARS-CoV-2, [10,11,18–27] and our group have previously demonstrated

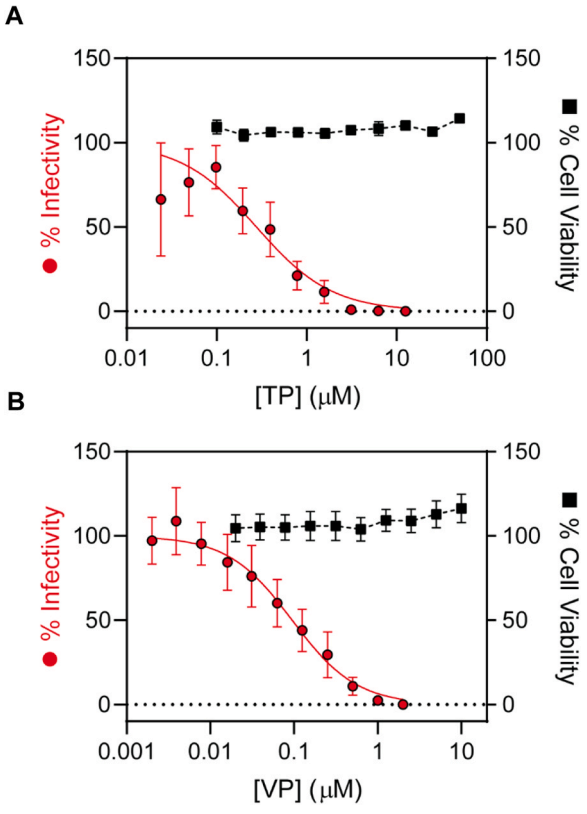

Fig. 2. - *In vitro* PDs light-independent SARS-CoV-2 inactivation and cytotoxicity in Caco-2 cells. To determine PDs IC50, SARS-CoV-2 infectious particles were incubated with different concentrations of (A) TP or (B) VP for 1 hour in the dark and viral infectivity was evaluated by plaque assay in Vero cells (red circles). For CC50 determination, non-infected Caco-2 cells were incubated with different concentrations of (A) TP or (B) VP for 24 hours and cytotoxicity was evaluated by resazurin reduction-based assays (black squares). Data are represented as means ± SEM for at least three independent samples.

that some porphyrins were able to inactivate different enveloped viruses, including DENV, ZIKV, and CHIKV in the dark, suggesting a broad spectrum antiviral activity for these class of molecules [10,11,18]. To prove temoporfin and verteporfin potential broad spectrum antiviral activity, we also tested these PDs light-independent anti-ZIKV activity (Supplementary Figure 2). Similarly to SARS-CoV-2 inactivation assays, ZIKV infectious particles were directly incubated with different concentrations of each PD for 1 hour in the dark. Infectivity yields of the treated viral particles were assessed by plaque assay. As expected, temoporfin and verteporfin were also active against ZIKV with IC50s of 276 ± 64 nM and 95 ± 21 nM, respectively (Table 1). Recently, non-photoactivated protoporphyrin IX, pyropheophorbide a and pheophorbide a were also described as promising anti-SARS-CoV-2 leads [23,46–48]. Gu et al., also described verteporfin anti-SARS-CoV-2 activity [47].

Furthermore, non-infected Caco-2 cells viability was determined by resazurin reduction-based assays, following temoporfin, verteporfin (Fig. 2), redaporfin or talaporfin (data not shown) 24-hour incubation in the dark. The calculated CC50 values are above 50 μM for temoporfin, redaporfin and talaporfin and above 10 μM for verteporfin (Table 1), values considered of safe prospective application given that CC50/IC50 ratios are higher than 26 and 107 for temoporfin and verteporfin, respectively.

Taken together, these findings support temoporfin and verteporfin

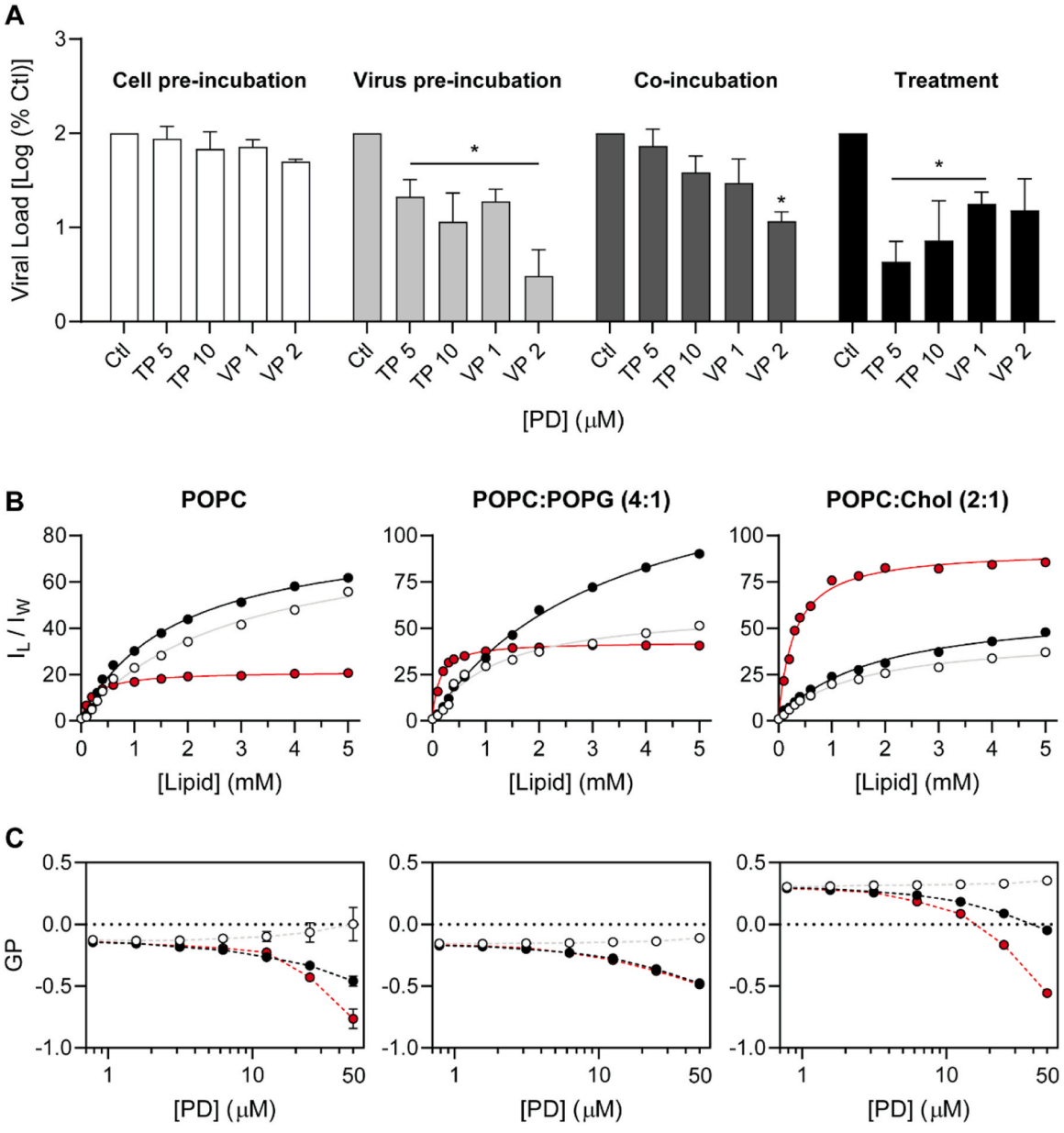

Fig. 3. - Mechanism of light-independent SARS-CoV-2 inactivation by clinically approved PDs. (A) Time-of-addition experiments were performed in Caco-2 cells. TP or VP were added to the cells (cell pre-incubation) or to the infectious viral particles (virus pre-incubation) for 1 hour prior to infection. Additionally, TP and VP were added to cells during (co-incubation) or immediately after (treatment) infection with SARS-CoV-2. Viral infectivity was evaluated by plaque assay 24 hours post infection. Data are represented as means ± SEM for at least three independent samples. * - Results with p-value ≤0.05 when compared with untreated control group. (B) Representative partition graphs for VP (red circles), TP (black circles) and RP (white circles). PDs fluorescence quantum yield was accessed upon titration with POPC (left-panel), POPC:POPG (middle-panel), or POPC:Chol (right-panel) LUVs. (C) Laurdan GPs upon crescent titration of VP (red circles), TP (black circles) and RP (white circles) in a fixed concentration of POPC (left-panel), POPC:POPG (middle-panel), or POPC:Chol (right-panel) LUVs. Data are represented as means ± SD for at least three independent samples.

potential broad-spectrum antiviral activity and low cytotoxicity, indicating their possible application not only in the treatment of COVID-19, but also in the treatment of other co-circulating viral infections.

3.3. Temoporfin and verteporfin act in early stages of viral replication

Incubation of SARS-CoV-2 and ZIKV with temoporfin and verteporfin resulted in loss of viral infectivity, suggesting that PDs interfere with viral particles ability to enter cells. To confirm this hypothesis, time-of-addition experiments were performed in Caco-2 cells (Fig. 3A). In agreement, pre-incubation of Caco-2 cells with both PDs did not hinder viral replication, while SARS-CoV-2 pre-incubation resulted in infection inhibition. Moreover, we also observed reduction in viral load when Caco-2 cells were incubated with verteporfin during virus absorption and entry (co-incubation). These data further confirm that temoporfin and verteporfin interfere in early stages of viral replication, probably through direct impact on the viral particles. PDs could induce viral particle disruption or affect viral particle structure, impairing virus-cell interaction processes such as fusion and entry. Noteworthy, Neris and colleagues showed that ZIKV treatment with Co-protoporphyrin IX and Sn-protoporphyrin IX resulted in a viral particle morphological changes, observed by transmission electron microscopy imaging [11].

Differently, temoporfin was described to inhibit ZIKV replication in human placental and neural progenitor cells by targeting flavivirus protease complex NS2B/NS3, potentially inhibiting viral polyprotein processing during ZIKV replication [49]. Indeed, SARS-CoV-2 load was also reduced when Caco-2 cells were treated, starting immediately after infection, with temoporfin and verteporfin for 24 hours (Fig. 3 A). Although, we cannot exclude PDs intracellular action during SARS-CoV-2 replication, the observed viral load reduction can also be explained by PDs interaction to viral infectious particles envelope. We propose that during each replication cycle, newly released viral particles are inactivated by PDs, impairing the next round of viral entry. In a longer timescale, the number of infectious viral particles is reduced, impacting infection yield as observed in Fig. 3 A. These results are in agreement with Assunção-Miranda et al., that also demonstrated that cell treatment with heme and Co-protoporphyrin IX during infection were able to reduce viral load, protecting cells from dengue virus-induced death [18]. Additionally, these data suggest that PDs, such as temoporfin and verteporfin, have therapeutic potential and could be used in viral disease control.

3.4. Temoporfin and verteporfin caused lipid order destabilization, which is responsible for their light-independent antiviral activity

It is well described that interaction/accumulation of some amphiphilic porphyrins in viral envelope lipid membranes disturb its structure, abrogating the early stages of viral infection, namely recognition, attachment and/or fusion with the host cell [10,11,17,25]. Temoporfin and verteporfin showed higher efficiency inhibiting the early stages of SARS-CoV-2 infection, which is in agreement with a direct action on the viral envelope structure. Concomitantly, the hydrophilic talaporfin did not present antiviral activity in the dark (Fig. 1D, right panel). Moreover, SARS-CoV-2 inactivation by some porphyrins and PDs was recently described and related to a direct effect on viral envelope [23,44,48]. Given these considerations, we evaluated temoporfin, verteporfin, talaporfin and redaporfin interaction with lipid membranes using LUVs as membrane models.

Lipid/water partition coefficients (K_ps) were calculated based on the increase in quantum yield of the PD fluorescence emission upon titration with LUVs [33,50]. Three lipid compositions were used: 1-palmitoyl-2-oleyl-sn-glycero-3-phosphatidylcholine (POPC) to mimic the zwitterionic outer leaflet of eukaryotic cell membranes (Fig. 3B, left panel), POPC and 1-palmitoyl-2-oleoyl-sn-glycero-3-phosphoglycerol (POPG) (4:1 molar) to mimic negatively charged inner leaflet of eukaryotic cell membranes (Fig. 3B, middle panel), and POPC and Cholesterol (Chol) (2:1 molar) to mimic rigid viral envelope membranes (Fig. 3B, right panel) [51–53]. Verteporfin, temoporfin and redaporfin fluorescence emission intensity increased in the presence of LUVs, indicating affinity towards all lipid compositions tested, at variance with talaporfin (data not shown). Talaporfin has four sodium carboxylate groups that increase its hydrophilicity [54], consequently decreasing or even nullifying its affinity towards lipid membranes. This result correlates with the lack of light-independent antiviral activity against SARS-CoV-2 demonstrated by this PD. Among the tested PDs, verteporfin presents the higher affinity towards all LUVs tested (Table 2), with K_p ranging 5.0–7.3 $\times 10^3$, i.e. circa one order magnitude higher than temoporfin and redaporfin, for which K_ps range from 0.4 to 0.6 $\times 10^3$ and from 0.5 to 1.1 $\times 10^3$, respectively. Verteporfin SARS-CoV-2 inactivation efficiency can be directly correlated to its higher affinity towards lipid membranes. However, the same direct relation cannot be assumed for temoporfin and redaporfin, given that for similar values of K_p, only temoporfin presents antiviral activity. It is worth mentioning that Marzorati *et al.* suggest that PDs uptake by membranes comprises two different phases: a first faster one corresponding to the electrostatically driven PDs adsorption to the amphiphilic outer membrane surface layer, and a second phase corresponding to the slower PD penetration into the non-polar membrane interior, both not only dependent on the PDs amphiphilicity but also on their overall polarity [55]. Redaporfin is a mixture of four atropisomers that differ in the orientation of the polar groups with respect to the macrocycle. Each atropisomer has approximately the same overall polarity but the amphiphilicities of the four atropisomers are different. In this case, it was shown that the most amphiphilic atropisomer uses a bind-flip mechanism to internalize cells faster than less amphiphilic atropisomers [56].

Since membrane affinity is not in itself the feature responsible for the PDs antiviral action, we further explored the capacity of the PDs to disturb membrane structure. PD-membrane destabilization was evaluated based on laurdan GP [34]. Lipid order variations induced by the PD lead to alterations in hydration, causing laurdan spectral shifts, which are reported by GP calculations. Significantly, only temoporfin and verteporfin, the two PD active in the dark, induce GP reduction in all lipid compositions tested (Fig. 3C). Lipid order destabilization is particularly noticeable on the viral-mimetic POPC:Chol (2:1) LUVs (Fig. 3C – right panel), where both temoporfin and verteporfin induce the transition of the majority phospholipid population from a gel phase (GP = 0.4) to a liquid-crystalline phase (GP = −0.5) [35]. In contrast, Meunier *et. al.* observations indicate that photoactivated pheophorbide a inactivates SARS-CoV-2 infectious particles by stiffening the viral envelope membrane [44], which suggest a different PD effect on viral envelope membrane in the presence of reactive oxygen species.

Although PDs antiviral activity is clearly dependent on membrane destabilization events, it was not clear why redaporfin does not present such destabilization effects. Redaporfin, like the antiviral-active temoporfin and verteporfin, is highly hydrophobic, presenting high membrane affinity. Variation on membrane penetration depth of some small molecules lead to different membrane local perturbations, that can impact their activity [57–59], which can be the case for the PDs. Thus, taking advantage of two lipophilic quenchers, fatty acids with a doxyl group on the 5th and 16th carbon of the aliphatic tails (5-NS and 16-NS, respectively), we calculated PDs membrane penetration depth (Z_{cF}) [36,60]. While redaporfin is located closer to the surface of the bilayer (10.4 Å from bilayer centre), consistent with the bind-flip mechanism

Table 2
PDs K_P and Z_{cF} values towards lipid membranes.

	K_P (x 10^3)			Z_{cF} (Å)
PD	POPC	POPC:POPG (4:1)	POPC:Chol (2:1)	
TP	0.5 ± 0.1	0.4 ± 0.05	0.6 ± 0.3	0.8
VP	7.1 ± 0.7	7.3 ± 1.2	5.0 ± 0.9	6.2
RP	0.5 ± 0.5	1.1 ± 0.3	0.8 ± 0.5	10.4

mentioned above, [56] both active PD temoporfin and verteporfin are located closer to the centre (0.8 and 6.2 Å from bilayer centre, respectively) (Table 2).

Overall, these results suggest that PDs light-independent anti-SARS-CoV-2 activity is mainly driven by three membrane-interaction properties, all uniquely shared by verteporfin and temoporfin: (1) high affinity towards lipid membranes, obviously being the first driver for the insertion on the viral envelope lipid bilayer; (2) deep membrane penetration; and (3) membrane destabilization capacity, causing variations on the viral envelope lipid packaging and fluidity, ultimately hindering all viral envelope membrane-dependent processes such as viral entry and/or fusion into the host cells. It is important to emphasize that the stated aspects of membrane interaction are probably not exclusive to viral envelope membranes, but rather that PDs also interact with healthy cell membranes because of their hydrophobic properties. However, in contrast to viruses, healthy cells membrane repairing pathways counteract the perturbations caused by PDs. This is in agreement with the low cytotoxicity of PDs towards Caco-2 cells. The same mechanistic features are also observed for others viral envelope-targeting antivirals [61–63].

At first glance, these results contradict Gu *et al.* observations, which suggest that verteporfin inhibited SARS-CoV-2 by binding to ACE2 and consequently interfering with the ACE2-S protein interaction [47]. In fact, negatively charged porphyrins can inhibit HIV entry through interaction with the V3 loop of gp120 [64–66]. Although we cannot exclude PDs interaction with ACE2, verteporfin ability to induce lipid order destabilization and inactivation of other enveloped virus, namely ZIKV, support the hypothesis of unspecific viral envelope targeting. Indeed, it has been established that porphyrins are able to interact and destabilize biological membranes and disrupt the functionality of the viral envelope as referred before [10,67].

4. Conclusions

COVID-19 pandemic left an immensurable socio-economic toll on world's population, where more than 7 million lives were lost. Even with the declaration of the end of the COVID-19 pandemic issued by WHO [68] efforts on finding alternative therapeutics for COVID-19 and the development of effective broad-spectrum antiviral therapies for future pandemics must continue. Porphyrins and PDs have been proposed as promising broad-spectrum antiviral molecules, and in here, we aimed to repurpose four PDs for the treatment of SARS-CoV-2 infection. Viral inactivation and further characterization of the active PDs antiviral mechanisms were presented.

As expected, all 4 PDs efficiently inactivated SARS-CoV-2 infection when photoactivated, which despite promising, is not particular suitable for a systemic treatment. Nonetheless, temoporfin and verteporfin were able to inactivate SARS-CoV-2 infectious particles in a light-independent manner, with IC50s in the nano-to-micromolar range. Beyond their viral inactivation potential, temoporfin and verteporfin significantly inhibited SARS-CoV-2 ongoing infection in Caco-2 cells, while not inducing cytotoxicity in non-infected cells, proving their potential for clinical application.

Since temoporfin and verteporfin inhibit the early stages of infection and considering the lipid-targeting mechanism already characterized for other porphyrins [10,11,18,23,25,44,48], a biophysical characterization of the PDs interaction with lipid membranes was performed. In this, high membrane affinity towards lipid vesicles, deep membrane penetration and enhanced membrane destabilization in membrane models revealed to be uniquely shared by temoporfin and verteporfin, in agreement with a viral envelope lipid membrane-targeting mechanism.

Finally, these results suggest temoporfin and verteporfin potential off-label application in the systemic treatment of COVID-19, with promising broad-spectrum application against emergent viruses.

Funding sources

This project has received funding from the European Union's Horizon 2020 research and innovation programme under grant agreement No 828774 and Fundação para a Ciência e a Tecnologia, I.P., through project RESEARCH4COVID n° 470, MOSTMICRO-ITQB R&D Unit (UIDB/04612/2020, UIDP/04612/2020), LS4FUTURE Associated Laboratory (LA/P/0087/2020) and iNOVA4Health R&D Unit (UIDB/04462/2020, UIDP/04462/2020). Additional funding from Fundação para a Ciência e a Tecnologia, I.P. is also acknowledged for D.A.M. (PD/BD/136752/2018); Í.C.-C. (PTDC/BIAVIR/29495/2017); C.C.B. (2022.13959.BD); Z.A.A (2021.09454.BD); FAS (PTDC/QUI -OUT/0303/2021).

CRediT authorship contribution statement

Diogo A. Mendonça: Writing – review & editing, Writing – original draft, Validation, Methodology, Investigation, Formal analysis, Conceptualization. **Iris Cadima-Couto:** Writing – review & editing, Validation, Methodology, Investigation, Formal analysis. **Carolina C. Buga:** Writing – review & editing, Investigation, Formal analysis. **Zoe A. Arnaut:** Writing – review & editing, Investigation, Formal analysis. **Fabio A. Schaberle:** Writing – review & editing, Methodology, Formal analysis. **Luis G. Arnaut:** Writing – review & editing, Resources, Methodology. **Miguel A. R. B. Castanho:** Writing – review & editing, Visualization, Validation, Supervision, Resources, Project administration, Methodology, Funding acquisition, Formal analysis, Conceptualization. **Christine Cruz-Oliveira:** Writing – review & editing, Writing – original draft, Visualization, Validation, Supervision, Project administration, Methodology, Investigation, Formal analysis, Conceptualization.

Declaration of Competing Interest

The authors declare that they have no known competing financial interests or personal relationships that could have appeared to influence the work reported in this paper.

Data Availability

Data will be made available on request.

Acknowledgements

The authors thank Pedro Simas Lab at Instituto de Medicina Molecular for providing the SARS-CoV-2 isolate used in this work and the Biosafety Level 3 Facility of Instituto de Medicina Molecular for their service and assistance.

Appendix A. Supporting information

Supplementary data associated with this article can be found in the online version at doi:10.1016/j.biopha.2024.116768.

References

[1] M. Marani, G.G. Katul, W.K. Pan, A.J. Parolari, Intensity and frequency of extreme novel epidemics, Proc. Natl. Acad. Sci. U. S. A. 118 (2021) e2105482118, https://doi.org/10.1073/pnas.2105482118.

[2] N. Zhu, D. Zhang, W. Wang, X. Li, B. Yang, J. Song, X. Zhao, B. Huang, W. Shi, R. Lu, P. Niu, F. Zhan, X. Ma, D. Wang, W. Xu, G. Wu, G.F. Gao, W. Tan, A novel coronavirus from patients with pneumonia in China, 2019, N. Engl. J. Med. 382 (2020) 727–733, https://doi.org/10.1056/nejmoa2001017.

[3] C. Huang, Y. Wang, X. Li, L. Ren, J. Zhao, Y. Hu, L. Zhang, G. Fan, J. Xu, X. Gu, Z. Cheng, T. Yu, J. Xia, Y. Wei, W. Wu, X. Xie, W. Yin, H. Li, M. Liu, Y. Xiao, H. Gao, L. Guo, J. Xie, G. Wang, R. Jiang, Z. Gao, Q. Jin, J. Wang, B. Cao, Clinical features of patients infected with 2019 novel coronavirus in Wuhan, China, Lancet 395 (2020) 497–506, https://doi.org/10.1016/S0140-6736(20)30183-5.

[4] P. V'kovski, A. Kratzel, S. Steiner, H. Stalder, V. Thiel, Coronavirus biology and replication: implications for SARS-CoV-2, Nat. Rev. Microbiol. 19 (2021) 155–170, https://doi.org/10.1038/s41579-020-00468-6.
[5] S. Xiu, A. Dick, H. Ju, S. Mirzaie, F. Abdi, S. Cocklin, P. Zhan, X. Liu, Inhibitors of SARS-CoV-2 entry: current and future opportunities, J. Med. Chem. 63 (2020) 12256–12274, https://doi.org/10.1021/acs.jmedchem.0c00502.
[6] A.C. Papageorgiou, I. Mohsin, The SARS-CoV-2 spike glycoprotein as a drug and vaccine target: structural insights into its complexes with ACE2 and antibodies, Cells 9 (2020), https://doi.org/10.3390/cells9112343.
[7] H. Abrahamse, M.R. Hamblin, New photosensitizers for photodynamic therapy, Biochem. J. 473 (2016) 347–364, https://doi.org/10.1042/BJ20150942.
[8] J.M. Dąbrowski, L.G. ArnautPhotodynamic therapy (PDT) of cancer: From local to systemic treatment, Photochem. Photobiol. Sci. 14 (2015), p. 1765–1780. https://doi.org/10.1039/c5pp00132c..
[9] L.L. Trannoy, F.G. Terpstra, D. De Korte, J.W.M. Lagerberg, A.J. Verhoeven, A. Brand, F.A.C. Van Engelenburg, Differential sensitivities of pathogens in red cell concentrates to Tri-P(4)-photoinactivation, Vox Sang. 91 (2006) 111–118, https://doi.org/10.1111/j.1423-0410.2006.00791.x.
[10] C. Cruz-Oliveira, A.F. Almeida, J.M. Freire, M.B. Caruso, M.A. Morando, V.N. S. Ferreira, I. Assunção-Miranda, A.M.O. Gomes, M.A.R.B. Castanho, A.T. Da Poian, Mechanisms of vesicular stomatitis virus inactivation by protoporphyrin IX, zinc-protoporphyrin IX, and mesoporphyrin IX, Antimicrob. Agents Chemother. 61 (2017), https://doi.org/10.1128/AAC.00053-17.
[11] R.L.S. Neris, C.M. Figueiredo, L.M. Higa, D.F. Araujo, C.A.M. Carvalho, B.R. F. Verçoza, M.O.L. Silva, F.A. Carneiro, A. Tanuri, A.M.O. Gomes, M.T. Bozza, A. T. Da Poian, C. Cruz-Oliveira, I. Assunção-Miranda, Co-protoporphyrin IX and Sn-protoporphyrin IX inactivate Zika, Chikungunya and other arboviruses by targeting the viral envelope, Sci. Rep. 8 (2018), https://doi.org/10.1038/s41598-018-27855-7.
[12] G. Basso, J.F. Cargnelutti, A.L. Oliveira, T.V. Acunha, R. Weiblen, E.F. Flores, B. A. Iglesias, Photodynamic inactivation of selected bovine viruses by isomeric cationic tetra-platinated porphyrins, J. Porphyr. Phthalocyanines 23 (2019) 1041–1046, https://doi.org/10.1142/S1088424619500767.
[13] L.L. Trannoy, J.W.M. Lagerberg, T.M.A.R. Dubbelman, H.J. Schuitmaker, Positively charged porphyrins: a new series of photosensitizers for sterilization of RBCs, Transfusion 44 (2004) 1186–1196, https://doi.org/10.1111/j.1537-2995.2004.03275.x.
[14] A. Almeida, M.A.F. Faustino, M.G.P.M.S. Neves, Antimicrobial photodynamic therapy in the control of COVID-19, Antibiotics 9 (2020) 1–10, https://doi.org/10.3390/antibiotics9060320.
[15] A.S. Ries, J.F. Cargnelutti, G. Basso, T.V. Acunha, B.A. Iglesias, E.F. Flores, R. Weiblen, Water-soluble tetra-cationic porphyrins display virucidal activity against Bovine adenovirus and Bovine alphaherpesvirus 1, Photo Photodyn. Ther. 31 (2020) 101947, https://doi.org/10.1016/j.pdpdt.2020.101947.
[16] E.M.P. Silva, F. Giuntini, M.A.F. Faustino, J.P.C. Tomé, M.G.P.M.S. Neves, A. C. Tomé, A.M.S. Silva, M.G. Santana-Marques, A.J. Ferrer-Correia, J.A.S. Cavaleiro, M.F. Caeiro, R.R. Duarte, S.A.P. Tavares, I.N. Pegado, B. D'Almeida, A.P.A. De Matos, M.L. Valdeira, Synthesis of cationic β-vinyl substituted meso-tetraphenylporphyrins and their in vitro activity against herpes simplex virus type 1, Bioorg. Med. Chem. Lett. 15 (2005) 3333–3337, https://doi.org/10.1016/j.bmcl.2005.05.044.
[17] J. Holoubek, J. Salát, J. Kotouček, T. Kastl, M. Vancová, I. Huvarová, P. Bednář, K. Bednářová, D. Růžek, D. Renčiuk, L. Eyer, Antiviral activity of porphyrins and porphyrin-like compounds against tick-borne encephalitis virus: Blockage of the viral entry/fusion machinery by photosensitization-mediated destruction of the viral envelope, Antivir. Res 221 (2024) 105767, https://doi.org/10.1016/j.antiviral.2023.105767.
[18] I. Assunção-Miranda, C. Cruz-Oliveira, R.L.S. Neris, C.M. Figueiredo, L.P.S. Pereira, D. Rodrigues, D.F.F. Araujo, A.T. Da Poian, M.T. Bozza, Inactivation of Dengue and Yellow Fever viruses by heme, cobalt-protoporphyrin IX and tin-protoporphyrin IX, J. Appl. Microbiol. 120 (2016) 790–804, https://doi.org/10.1111/jam.13038.
[19] F.J. Benati, F. Lauretti, L.C. Faccin, B. Nodari, D.V. Ferri, M.S. Mantovani, R.E. C. Linhares, C. Nozawa, Effects of chlorophyllin on replication of poliovirus and bovine herpesvirus in vitro, Lett. Appl. Microbiol. 49 (2009) 791–795, https://doi.org/10.1111/j.1472-765X.2009.02744.x.
[20] D.W. Dixon, A.F. Gill, L. Giribabu, A.N. Vzorov, A.B. Alam, R.W. Compans, Sulfonated naphthyl porphyrins as agents against HIV-1, J. Inorg. Biochem. 99 (2005) 813–821, https://doi.org/10.1016/j.jinorgbio.2004.12.013.
[21] H. Guo, X. Pan, R. Mao, X. Zhang, L. Wang, X. Lu, J. Chang, J.T. Guo, S. Passic, F. C. Krebs, B. Wigdahl, T.K. Warren, C.J. Retterer, S. Bavari, X. Xu, A. Cuconati, T. M. Block, Alkylated porphyrins have broad antiviral activity against hepadnaviruses, flaviviruses, filoviruses, and arenaviruses, Antimicrob. Agents Chemother. 55 (2011) 478–486, https://doi.org/10.1128/AAC.00989-10.
[22] A.N. Vzorov, D.W. Dixon, J.S. Trommel, L.G. Marzilli, R.W. Compans, Inactivation of Human Immunodeficiency Virus Type 1 by, Porphyrins 46 (2002) 3917–3925, https://doi.org/10.1128/aac.46.12.3917-3925.2002.
[23] S. Lu, X. Pan, D. Chen, X. Xie, Y. Wu, W. Shang, X. Jiang, Y. Sun, S. Fan, J. He, Broad-spectrum antivirals of protoporphyrins inhibit the entry of highly pathogenic emerging viruses, Bioorg. Chem. 107 (2021), https://doi.org/10.1016/j.bioorg.2020.104619.
[24] Y. Cheng, L.K. Tsou, J. Cai, T. Aya, G.E. Dutschman, E. a Gullen, S.P. Grill, A.P. C. Chen, B.D. Lindenbach, A.D. Hamilton, Y.C. Cheng, A novel class of meso-tetrakis-porphyrin derivatives exhibits potent activities against hepatitis C virus genotype 1b replicons in vitro, Antimicrob. Agents Chemother. 54 (2010) 197–206, https://doi.org/10.1128/AAC.01206-09.
[25] M.M. Xu, B. Wu, G.G. Huang, C.L. Feng, X.H. Wang, H.Y. Wang, Y.W. Wu, W. Tang, Hemin protects against Zika virus infection by disrupting virus-endosome fusion, Antivir. Res 203 (2022) 105347, https://doi.org/10.1016/J.ANTIVIRAL.2022.105347.
[26] D. Sengupta, M. Rai, Z. Hoque Mazumdar, D. Sharma, K. Malabika Singha, P. Pandey, R. Gaur, Two cationic meso-thiophenium porphyrins and their zinc-complexes as anti-HIV-1 and antibacterial agents under non-photodynamic therapy (PDT) conditions, Bioorg. Med. Chem. Lett. 65 (2022) 128699, https://doi.org/10.1016/j.bmcl.2022.128699.
[27] D. Sengupta, U. Timilsina, Z.Hoque Mazumder, A. Mukherjee, D. Ghimire, M. Markandey, K. Upadhyaya, D. Sharma, N. Mishra, T. Jha, S. Basu, R. Gaur, Dual activity of amphiphilic Zn(II) nitroporphyrin derivatives as HIV-1 entry inhibitors and in cancer photodynamic therapy, (2019), doi:10.1016/j.ejmech.2019.04.051.
[28] R. Baskaran, J. Lee, S.-G. Yang, Clinical development of photodynamic agents and therapeutic applications, Biomater. Res. 22 (2018), https://doi.org/10.1186/s40824-018-0140-z.
[29] M.A. Rajora, J.W.H. Lou, G. Zheng, Advancing porphyrin's biomedical utility: via supramolecular chemistry, Chem. Soc. Rev. 46 (2017) 6433–6469, https://doi.org/10.1039/c7cs00525c.
[30] L.G. Arnaut, M.M. Pereira, Overcoming the challenges of infrared photosensitizers in photodynamic therapy: the making of redaporfin, Chem. Commun. 59 (2023) 9457–9468, https://doi.org/10.1039/d3cc02283h.
[31] F.A. Schaberle, Assessment of the actual light dose in photodynamic therapy, Photo Photodyn. Ther. 23 (2018) 75–77, https://doi.org/10.1016/j.pdpdt.2018.06.009.
[32] S. Vemuri, C.T. Rhodes, Preparation and characterization of liposomes as therapeutic delivery systems: a review, Pharm. Acta Helv. 70 (1995) 95–111, https://doi.org/10.1016/0031-6865(95)00010-7.
[33] N.C. Santos, M. Prieto, M.A.R.B. Castanho, Quantifying molecular partition into model systems of biomembranes: an emphasis on optical spectroscopic methods, Biochim. Biophys. Acta - Biomembr. 1612 (2003) 123–135, https://doi.org/10.1016/S0005-2736(03)00112-3.
[34] T. Parasassi, E. Gratton, Membrane lipid domains and dynamics as detected by Laurdan fluorescence, J. Fluoresc. 5 (1995) 59–69, https://doi.org/10.1007/BF00718783.
[35] S.A. Sanchez, M.A. Tricerri, E. Gratton, Laurdan generalized polarization fluctuations measures membrane packing micro-heterogeneity in vivo, Proc. Natl. Acad. Sci. U. S. A. 109 (2012) 7314–7319, https://doi.org/10.1073/pnas.1118288109.
[36] F.S. Abrams, E. London, Calibration of the parallax fluorescence quenching method for determination of membrane penetration depth: refinement and comparison of quenching by spin-labeled and brominated lipids, Biochemistry 31 (1992) 5312–5322, https://doi.org/10.1021/bi00138a010.
[37] M.X. Fernandes, J. García De La Torre, M.A.R.B. Castanho, Joint determination by Brownian dynamics and fluorescence quenching of the in-depth location profile of biomolecules in membranes, Anal. Biochem. 307 (2002) 1–12, https://doi.org/10.1016/S0003-2697(02)00024-6.
[38] F. Stauffer, M.N. Melo, F.A. Carneiro, F.J.R. Sousa, M.A. Juliano, L. Juliano, R. Mohana-Borges, A.T. Da Poian, M.A.R.B. Castanho, Interaction between dengue virus fusion peptide and lipid bilayers depends on peptide clustering, Mol. Membr. Biol. 25 (2008) 128–138, https://doi.org/10.1080/09687680701633091.
[39] B.A. Lewis, D.M. Engelman, Lipid bilayer thickness varies linearly with acyl chain length in fluid phosphatidylcholine vesicles, J. Mol. Biol. 166 (1983) 211–217, https://doi.org/10.1016/S0022-2836(83)80007-2.
[40] R.T. Aroso, F.A. Schaberle, L.G. Arnaut, M.M. Pereira, Photodynamic disinfection and its role in controlling infectious diseases, Springe Int. Publ. (2021), https://doi.org/10.1007/s43630-021-00102-1.
[41] L. Pires, B.C. Wilson, R. Bremner, A. Lang, J. Larouche, R. McDonald, J.D. Pearson, D. Trcka, J. Wrana, J. Wu, C.M. Whyne, R. Romanow, Provincial Laboratory, S. Health Authority, H. Bone, J. Program, Translational feasibility and efficacy of nasal photodynamic disinfection of SARS-CoV-2, Sci. Rep. 12 (2020) 14438, https://doi.org/10.1038/s41598-022-18513-0.
[42] V.A. Svyatchenko, S.D. Nikonov, A.P. Mayorov, M.L. Gelfond, V.B. Loktev, Antiviral photodynamic therapy: inactivation and inhibition of SARS-CoV-2 in vitro using methylene blue and Radachlorin, Photo Photodyn. Ther. 33 (2021) 68, https://doi.org/10.1016/j.pdpdt.2020.102112.
[43] Z.A. Arnaut, S.M.A. Pinto, R.T. Aroso, A.S. Amorim, C.S. Lobo, F.A. Schaberle, D. Pereira, J. Núñez, S.C.C. Nunes, A.A.C.C. Pais, P. Rodrigues-Santos, L.P. de Almeida, M.M. Pereira, L.G. Arnaut, Selective, broad-spectrum antiviral photodynamic disinfection with dicationic imidazolyl chlorin photosensitizers, Photochem. Photobiol. Sci. (2023), https://doi.org/10.1007/s43630-023-00476-4.
[44] T. Meunier, L. Desmarets, S. Bordage, M. Bamba, K. Hervouet, Y. Rouillé, N. François, M. Decossas, V. Sencio, F. Trottein, F.H.T. Bi, O. Lambert, J. Dubuisson, S. Belouzard, S. Sahpaz, K. Séron, A photoactivable natural product with broad antiviral activity against enveloped viruses, including highly pathogenic coronaviruses, Antimicrob. Agents Chemother. 66 (2022), https://doi.org/10.1128/AAC.01581-21.
[45] D. Schikora, J. Hepburn, S.R. Plavin, L. Health, Reduction of the viral load by non-invasive photodynamic therapy in early stages of COV-ID-19 infection, Am. J. Virol. Dis. 2 (2020) 01–05.
[46] G.H. Jimenez-Aleman, V. Castro, A. Londaitsbehere, M. Gutierrez-Rodríguez, U. Garaigorta, R. Solano, P. Gastaminza, SARS-CoV-2 Fears Green: The Chlorophyll Catabolite Pheophorbide A Is a Potent Antiviral, (2021), doi:10.3390/ph14101048.
[47] C. Gu, Y. Wu, H. Guo, Y. Zhu, W. Xu, Y. Wang, Y. Zhou, Protoporphyrin IX and verteporfin potently inhibit SARS-CoV-2 infection in vitro and in a mouse model expressing human ACE2, (2020), doi:10.1016/j.scib.2020.12.005.

[48] D. Chen, S. Lu, G. Yang, X. Pan, S. Fan, X. Xie, Q. Chen, F. Li, Z. Li, S. Wu, J. He, The seafood Musculus senhousei shows anti-influenza A virus activity by targeting virion envelope lipids, Biochem. Pharmacol. 177 (2020) 113982, https://doi.org/10.1016/j.bcp.2020.113982.

[49] Z. Li, M. Brecher, Y.Q. Deng, J. Zhang, S. Sakamuru, B. Liu, R. Huang, C. A. Koetzner, C.A. Allen, S.A. Jones, H. Chen, N.N. Zhang, M. Tian, F. Gao, Q. Lin, N. Banavali, J. Zhou, N. Boles, M. Xia, L.D. Kramer, C.F. Qin, H. Li, Existing drugs as broad-spectrum and potent inhibitors for Zika virus by targeting NS2B-NS3 interaction, Cell Res 27 (2017) 1046–1064, https://doi.org/10.1038/cr.2017.88.

[50] J.M. Freire, M.M. Domingues, J. Matos, M.N. Melo, A.S. Veiga, N.C. Santos, M. a R. B. Castanho, Using zeta-potential measurements to quantify peptide partition to lipid membranes, Eur. Biophys. J. 40 (2011) 481–487, https://doi.org/10.1007/s00249-010-0661-4.

[51] B. Fadeel, D. Xue, The ins and outs of phospholipid asymmetry in the plasma membrane: roles in health and disease, Crit. Rev. Biochem. Mol. Biol. 44 (2009) 264–277, https://doi.org/10.1080/10409230903193307.

[52] S. Bajimaya, T. Frankl, T. Hayashi, T. Takimoto, Cholesterol is required for stability and infectivity of influenza A and respiratory syncytial viruses, Virology 510 (2017) 234–241, https://doi.org/10.1016/j.virol.2017.07.024.

[53] M. Veit, B. Thaa, Association of influenza virus proteins with membrane rafts, Adv Virol. 2011 (2011), https://doi.org/10.1155/2011/370606.

[54] S. Wang, E. Bromley, L. Xu, J.C. Chen, L. Keltner, Talaporfin sodium, Expert Opin. Pharmacother. 11 (2010) 133–140, https://doi.org/10.1517/14656560903463893.

[55] M. Marzorati, P. Bigler, M. Vermathen, Interactions between selected photosensitizers and model membranes: An NMR classification, Biochim. Biophys. Acta - Biomembr. 1808 (2011) 1661–1672, https://doi.org/10.1016/j.bbamem.2011.02.011.

[56] C. Donohoe, F.A. Schaberle, F.M.S. Rodrigues, N.P.F. Gonçalves, C.J. Kingsbury, M. M. Pereira, M.O. Senge, L.C. Gomes-Da-Silva, L.G. Arnaut, Unraveling the pivotal role of atropisomerism for cellular internalization, J. Am. Chem. Soc. 144 (2022) 15252–15265, https://doi.org/10.1021/jacs.2c05844.

[57] L. Dupou-Cézanne, A. -M. Saufereau, J. -F. Tocanne, Localization of adriamycin in model and natural membranes: Influence of lipid molecular packing, Eur. J. Biochem. 181 (1989) 695–702, https://doi.org/10.1111/j.1432-1033.1989.tb14779.x.

[58] D.A. García, M.A. Perillo, Benzodiazepine localisation at the lipid-water interface: effect of membrane composition and drug chemical structure, Biochim. Biophys. Acta - Biomembr. 1418 (1999) 221–231, https://doi.org/10.1016/S0005-2736(99)00040-1.

[59] C.B. Fox, R.A. Horton, J.M. Harris, Detection of drug-membrane interactions in individual phospholipid vesicles by confocal Raman microscopy, Anal. Chem. 78 (2006) 4918–4924, https://doi.org/10.1021/ac0605290.

[60] A.S. Ladokhin, Measuring membrane penetration with depth-dependent fluorescence quenching: distribution analysis is coming of age, Biochim. Biophys. Acta - Biomembr. 1838 (2014) 2289–2295, https://doi.org/10.1016/j.bbamem.2014.02.019.

[61] M.C. Wolf, A.N. Freiberg, T. Zhang, Z. Akyol-Ataman, A. Grock, P.W. Hong, J. Li, N.F. Watson, A.Q. Fang, H.C. Aguilar, M. Porotto, A.N. Honko, R. Damoiseaux, J. P. Miller, S.E. Woodson, S. Chantasirivisal, V. Fontanes, O. a Negrete, P. Krogstad, A. Dasgupta, A. Moscona, L.E. Hensley, S.P. Whelan, K.F. Faull, M.R. Holbrook, M. E. Jung, B. Lee, A broad-spectrum antiviral targeting entry of enveloped viruses, Proc. Natl. Acad. Sci. U. S. A. 107 (2010) 3157–3162, https://doi.org/10.1073/pnas.0909587107.

[62] F. Vigant, J. Lee, A. Hollmann, L.B. Tanner, Z. Akyol Ataman, T. Yun, G. Shui, H. C. Aguilar, D. Zhang, D. Meriwether, G. Roman-Sosa, L.R. Robinson, T.L. Juelich, H. Buczkowski, S. Chou, M. a R.B. Castanho, M.C. Wolf, J.K. Smith, A. Banyard, M. Kielian, S. Reddy, M.R. Wenk, M. Selke, N.C. Santos, A.N. Freiberg, M.E. Jung, B. Lee, A mechanistic paradigm for broad-spectrum antivirals that target virus-cell fusion, PLoS Pathog. 9 (2013), https://doi.org/10.1371/journal.ppat.1003297.

[63] F. Vigant, N.C. Santos, B. Lee, Broad-spectrum antivirals against viral fusion, Nat. Rev. Microbiol. 13 (2015) 426–437, https://doi.org/10.1038/nrmicro3475.

[64] K. Watanabe, S. Negi, Y. Sugiura, A. Kiriyama, A. Honbo, K. Iga, E.N. Kodama, T. Naitoh, M. Matsuoka, K. Kano, Binding of multivalent anionic porphyrins to V3 loop fragments of an HIV-1 envelope and their antiviral activity, Chem. - Asian J. 5 (2010) 825–834, https://doi.org/10.1002/asia.200900465.

[65] a R. Neurath, N. Strick, a K. Debnath, Structural requirements for and consequences of an antiviral porphyrin binding to the V3 loop of the human immunodeficiency virus (HIV-1) envelope glycoprotein gp120, J. Mol. Recognit. 8 (1995) 345–357, https://doi.org/10.1002/jmr.300080604.

[66] A.K. Debnath, S. Jiang, N. Strick, K. Lin, P. Haberfield, A.R. Neurath, Three-Dimensional Structure-Activity Analysis of a Series of Porphyrin Derivatives with Anti-HIV-1 Activity Targeted to the V3 Loop of the gp120 Envelope Glycoprotein of the Human Immunodeficiency Virus Type 1, J. Med. Chem. 37 (1994) 1099–1108, https://doi.org/10.1021/jm00034a007.

[67] T.H. Schmitt, W. a Frezzatti, S. Schreier, Hemin-induced lipid membrane disorder and increased permeability: a molecular model for the mechanism of cell lysis, Arch. Biochem. Biophys. 307 (1993) 96–103, https://doi.org/10.1006/abbi.1993.1566.

[68] World Health Organization, Statement on the fifteenth meeting of the IHR (2005) Emergency Committee on the COVID-19 pandemic, (n.d.). https://www.who.int/news/item/05–05-2023-statement-on-the-fifteenth-meeting-of-the-international-health-regulations-(2005)-emergency-committee-regarding-the-coronavirus-disease-(covid-19)-pandemic.